Experimentally tractable generation of high-order rogue waves in Bose-Einstein condensates

J. Adriazola[1,2] and P. G. Kevrekidis[2,3]

[1]*Department of Mathematics, Southern Methodist University, Dallas, Texas, USA*
[2]*Department of Physics, University of Massachusetts, Amherst, Massachusetts 01003, USA*
[3]*Department of Mathematics and Statistics, University of Massachusetts Amherst, Amherst, Massachusetts 01003-4515, USA*

In this work, we study a prototypical, experimentally accessible scenario that enables the systematic generation of so-called high-order rogue waves in atomic Bose-Einstein condensates. These waveforms lead to *significantly* and *controllably* more extreme focusing events than the famous Peregrine soliton. In one spatial dimension, we showcase conclusive numerical evidence that our scheme generates the focusing behavior associated with the first four rogue waves from the relevant hierarchy. We then extend considerations to anisotropic two-dimensional and even three-dimensional settings, establishing that the scheme can generate second-order rogue waves despite the well-known limitation of finite-time blow up of focusing nonlinear Schrödinger equations.

I. INTRODUCTION

Over the last two decades, the study of rogue waves has become one of the most active themes of study within nonlinear science [1–6]. A series of remarkable developments, initially in the field of nonlinear optics [7–13], led to detection tools for probing rogue waves and also suggested their relevance in other applications, such as in supercontinuum generation. Meanwhile, state-of-the-art experiments in fluid mechanics [14–16] not only enabled the realization of the famous prototypical Peregrine soliton nonlinear waveform [17], but also a higher-order breather referred to as a "super rogue wave" [15]. Importantly, other areas of dispersive wave dynamics including plasmas [18–20] and more recently atomic Bose-Einstein condensates [21] have offered additional fertile platforms for the exploration of associated rogue wave dynamics.

What is perhaps less familiar in the physics community is how these rogue waves naturally emerge in different wave-breaking scenarios of dispersive wave partial differential equation (PDE) models. Here, we argue that such an understanding proves essential to their physical implementation and immediately provides an experimentally tractable example. Starting with the universal Korteweg–de Vries equation, a famous Dubrovin conjecture proved in [22] characterized wave breaking as described by a solution of the second member of the Painlevé-I hierarchy. Similarly, for the universal nonlinear Schrödinger (NLS) model, the proof of another Dubrovin conjecture in [23] established the wave-breaking description via a solution of the the tritronquée solution of the Painlevé-I equation. The work of [24] obtained similar results for the Sine-Gordon model.

Our focus herein involves a less generic, yet still very much experimentally tractable scenario involving the NLS equation, a ubiquitous physics model that arises in nonlinear optics [25,26], atomic physics [27–29], and plasma dynamics [30]. The NLS equation features a nongeneric focusing example based on a Painlevé-III-type breaking known to arise from the so-called Talanov, or semi-circle, initial data [31,32]. As recently explained in [33], the dispersionless limit of this

problem exhibits a finite-time blow up with the presence of dispersion manifesting so-called high-order rogue waves (HORWs). The authors of [34] showed how HORWs can be obtained via Darboux transformations while the authors of [35,36] provided a more mathematically detailed study thereof; see also [37] for a more physically minded review. Indeed, this process has an asymptotic limit, namely, the so-called infinite-order rogue wave that was identified, for the first time to our knowledge, in the work of [38].

Our aim is to show that atomic Bose-Einstein condensates present an excellent opportunity for the generation of high-order, and potentially infinite-order, rogue waves dynamically. This is due to the fact that in the well-known Thomas-Fermi (TF) limit of large density, such systems under self-defocusing (self-repulsive) nonlinearity acquire a well-established parabolic density profile [27–29], up to a small boundary-layer and curvature-driven correction that has been analyzed in [39,40].

This provides approximately semi-circular initial wave-function data "for free," as it is the ground state of the self-repulsive problem provided that one can perform a quench in the nonlinearity from the defocusing to the focusing, modulationally unstable regime. Fortunately, such quenches are known to be quite feasible in atomic Bose-Einstein condensates (BECs), from the early works of [41,42], to demonstrations of wide tunability in [43], and even the recent realization of Townes soliton collapse in [44]. Indeed, such a quench was proposed towards creating a fundamental (Peregrine) rogue wave in [45]. Furthermore, the very recent work of [46] used such a quench to probe the collapse of a vortical BEC pattern.

We show that this technique can be tuned through the chemical potential, the trap strength, and the scattering length to provide good approximations of kth-order rogue waves for $k = 2$, $k = 3$, and $k = 4$, with the potential to, in principle, generalize this approach to higher orders. We then go beyond one-dimensional settings, as is more realistic in atomic BECs, and illustrate that even higher-dimensional settings with a quasi-one-dimensional (1D) confinement *still* provide the

possibility of an excitation of higher-order rogue waves such as $k = 2$ and $k = 3$. This, in turn, strongly suggests that many of the above experiments bear the controllable formation of such higher-order rogue waves at their fingertips and the experimental range to which this technology can be used to obtain excitations of large amplitude waveforms still remains to be (hopefully, imminently) explored.

II. THEORETICAL ANALYSIS OF HORWs

To briefly provide the theoretical background of the type of rogue waves that we consider throughout this work, we closely follow the concise account of Bilman *et al.* [35]. We begin by considering the prototypical focusing NLS equation

$$i\partial_t \psi = -\tfrac{1}{2}\partial_x^2 \psi - |\psi|^2 \psi, \qquad (1)$$

where $x \in \mathbb{R}$. A potential term $V(x)\psi$ added to the right-hand side of Eq. (1) will also (when appropriate) be considered in the numerical examples that follow. Notice that for all considerations below, for breadth of exposition, we will maintain our quantities dimensionless. Numerous systematic topical expositions, e.g., in atomic physics [27–29] or optics [25,26] detail how to translate these general findings to dimensional units, as needed.

An expression of the HORWs that exactly solve the NLS equation (1) can be constructed through the following procedure. Consider the expansion coefficients from the suitable series expansion around $\lambda = i$, $F_\ell(x, t)$ and $G_\ell(x, t)$, where $\ell \in \mathbb{Z}^+$, arising from the generating functions

$$(1 - i\lambda)\frac{\sin((x + \lambda t)\sqrt{\lambda^2 + 1})}{\sqrt{\lambda^2 + 1}} = \sum_{\ell=0}^{\infty}\left(\frac{i}{2}\right)^\ell F_\ell(x, t)(\lambda - i)^\ell,$$

$$\cos((x + \lambda t)\sqrt{\lambda^2 + 1}) = \sum_{\ell=0}^{\infty}\left(\frac{i}{2}\right)^\ell G_\ell(x, t)(\lambda - i)^\ell.$$

We use these coefficients to define the following $k \times k$ matrices

$$K_{pq}^{(k)}(x, t)$$
$$:= \sum_{\mu=0}^{p-1}\sum_{v=0}^{q-1}\binom{\mu + v}{\mu}(F_{q-v-1}^* F_{p-\mu-1} + G_{q-v-1}^* G_{p-\mu-1}),$$

and

$$H_{pq}^{(k)}(x, t) := -2(F_{p-1} + G_{p-1})(F_{q-1}^* - G_{q-1}^*),$$

where $1 \leqslant p, q \leqslant k$ and with $*$ denoting complex conjugation, while the arguments of F and G, being (x, t), are implied for brevity.

Rogue waves of order k, denoted by $\psi_k(x, t)$, are furnished by the following formula:

$$\psi_k(x, t) := (-1)^k \frac{\det(\mathbf{K}^{(k)}(x, t) + \mathbf{H}^{(k)}(x, t))}{\det(\mathbf{K}^{(k)}(x, t))}. \qquad (2)$$

For example, the $k = 1$ Peregrine solution, up to an unimportant phase factor, is given by

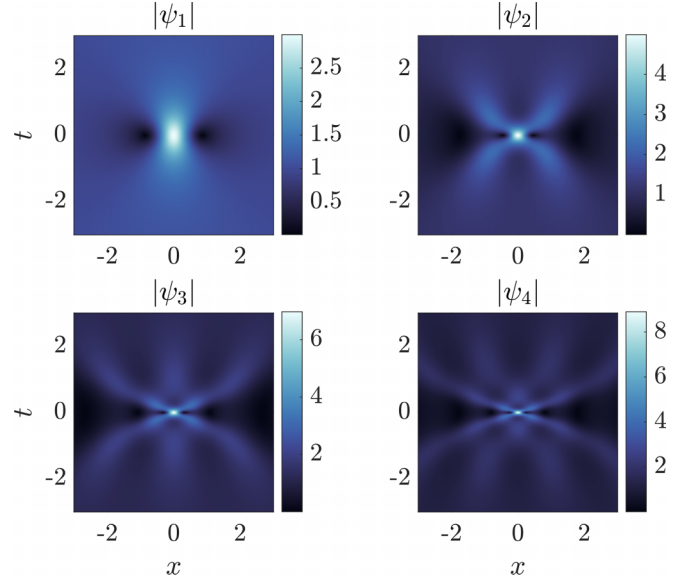$$\psi_1(x, t) := 1 - 4\frac{1 + 2it}{1 + 4x^2 + 4t^2}.$$

FIG. 1. Visualization of the first four NLS rogue waves, in absolute value, whose formulas are given by Eq. (2) and the immediately preceding definitions.

The compact representation afforded by Eq. (2) coincides with the leading order solution of a parametrized matrix Riemann-Hilbert problem. See [35], in particular Proposition 1, for more details.

We show the space-time evolution of the first four of these rogue waves, in absolute value, in Fig. 1. Note that this process can be generalized for arbitrary k, leading eventually to the limit of $k \to \infty$ which corresponds to the waveform discovered in [38]. The sequence of the states, through having k "stems" and from which an extreme focusing emerges, is transparent in the space-time evolution of the patterns in Fig. 1.

III. NUMERICAL EXAMPLES: ONE-DIMENSIONAL CASE

We now turn to the one-dimensional realization of our proposed experimental protocol (within atomic BECs [27–29]).

We start at the defocusing regime with a parabolic confinement $V(x) = (1/2)\Omega^2 x^2$ and nonlinear defocusing prefactor g_{defocus}, for a controllable chemical potential μ; both μ and Ω are tunable, and $\mu \gg \Omega$ defines the effective TF regime. The ground-state wave function is approximately semicircular with density controllably approximated by $|\psi_{\text{TF}}|^2 = \mu - V(x)$, where $\mu > V(x)$. The approximation becomes progressively better as the TF regime is approached, with an accordingly shrinking boundary layer (see also [39,40]).

Now, at $t = 0$, we switch the nonlinearity to a focusing one of prefactor g_{focus}, i.e., solving Eq. (1), but with (again, controllable attractive interactions [42,43,47]) nonlinear prefactor g_{focus} and through this protocol controllably close to a semi-circular initial condition. We use imaginary-time propagation [48] to compute the ground state with evolution, here and in the focusing case, computed via an adaptive step-size split-step method [49] (see Appendix B for more details). To summarize, we present the entire protocol succinctly in two steps.
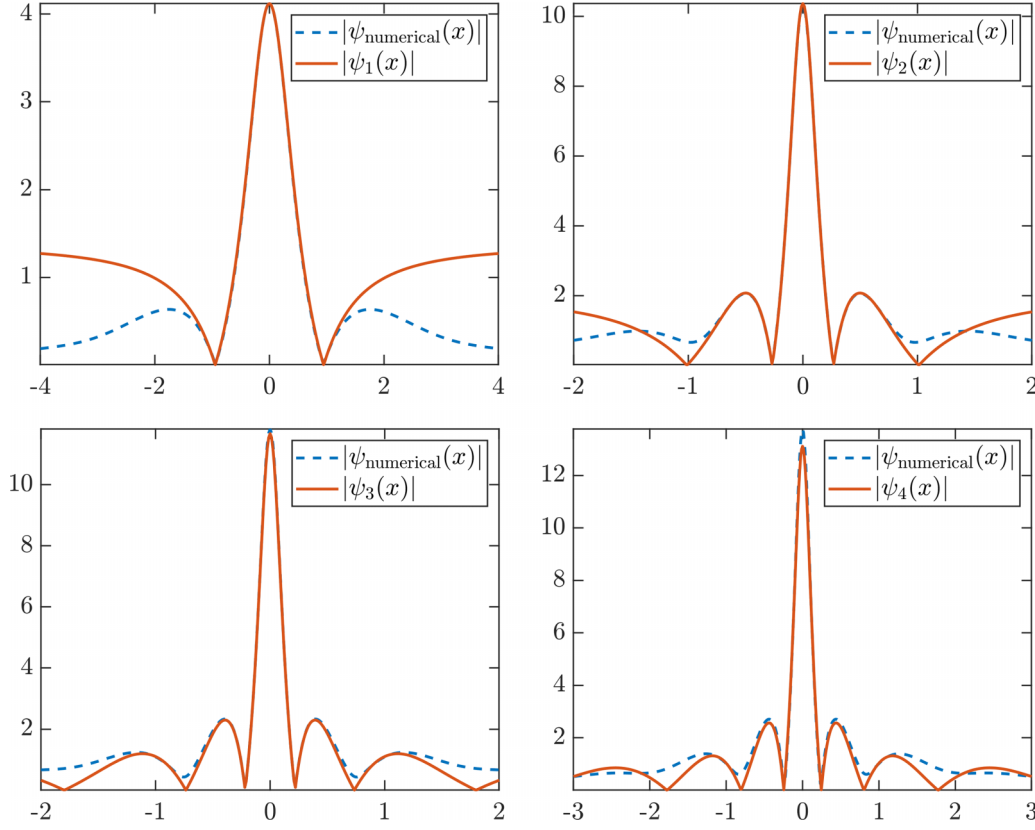
FIG. 2. Local fitting of our numerical simulations to the first 4 (i.e., $k = 1$ to $k = 4$) HORWs given by Eq. (2). We report the parameters $p = (\Omega, g_{\text{defocus}}, g_{\text{focus}}, \mu, s)$ to three digits of precision. Top left: $(1.06, 0.87, -0.443, 3.42, 0.914)$. Top right: $(1.23, 0.891, -0.701, 6.19, 1.74)$. Bottom left: $(1.25, 1.07, -0.794, 7.42, 1.49)$. Bottom right: $(1.93, 1.84, -0.483, 18.2, 1.01)$.

Step 1: For a given chemical potential μ, a trap strength Ω, and *defocusing* parameter $g_{\text{defocus}} > 0$, compute the ground state $\varphi_0(x)$ of the defocusing steady-state equation $\mu\psi = -\frac{1}{2}\partial_x^2\psi + g_{\text{defocus}}|\psi|^2\psi + \frac{\Omega^2}{2}x^2\psi$.

Step 2: For a given *focusing* parameter $g_{\text{focus}} > 0$, release the trap and use $\varphi_0(x)$ as the initial condition in the focusing dynamics given by $i\partial_t\psi = -\frac{1}{2}\partial_x^2\psi - g_{\text{focus}}|\psi|^2\psi$.

To make the claim that this protocol enables the controlled generation (as the parameters μ, g, and Ω are varied) of high-order rogue waves, we perform a fit of our numerical realizations thereof, at the time of maximal focusing, to the exact solutions given by Eq. (2) rescaled appropriately in space and by the value of the nonlinear focusing coefficient g_{focus} such that the NLS equation (1) remains invariant. We denote the rescaling in space used to minimize the mismatch in an L^2 norm between the numerics and the exact solution by the symbol s. Since the functions given by Eq. (2) have a nonzero background, we minimize a mismatch centered at space and with a spatial extent that terminates where the absolute value of $|\psi|$ reaches its last local minimum to the left and to the right of the origin. Denote this spatial region as ζ.

Thus, as a computational problem, the entirety of our work here is a search for the vector $p = (\Omega, g_{\text{defocus}}, g_{\text{focus}}, \mu, s)$ that optimizes (i.e., minimizes) the relative mismatch

$$\mathcal{M}(p) = \frac{\left|\|\psi_p\|^2_{L^2(\zeta)} - \|\psi_k\|^2_{L^2(\zeta)}\right|}{\|\psi_k\|^2_{L^2(\zeta)}}, \qquad (3)$$

where ψ_k is the kth-order rogue wave given by Eq. (2) and ψ_p is the wave function corresponding to the observed density at the maximal focusing time and generated from our protocol from the five-dimensional parameter vector p. It is important to reiterate here that the wide range of available choices of $\Omega \ll 1$ and μ are made so as to place us in a suitably elongated 1D regime such that the TF approximation is a meaningful one along this dimension. Such considerations will reflect our choices of trap frequencies and chemical potential also for the higher-dimensional anisotropic traps below). To solve the optimization problem $\min_p \mathcal{M}(p)$, we use differential evolution methods, as discussed, e.g., in [50].

In Fig. 2, we report the parameters p found through the minimization and show the match, in absolute value to facilitate visualization, between the first four generated rogue waves and the exact expressions from Eq. (2). Naturally, and similarly to what occurs in the case of the single Peregrine in BECs [21], we can only hope to *locally* match the kth-order rogue waves, given the distinct nature of the spatial asymptotics of our initial conditions, hence the need for our proposed matching selection. Nevertheless, our fitting procedure clearly suggests the local spontaneous generation of the relevant multihump patterns, by analogy with what happens for Peregrine-based wave breaking in [23]. Moreover, we demonstrate numerically, in Appendix A, that our experimental protocol shows great promise for remaining robust against uncertainties in the parameter vector p (relevant to potential experimental factors).
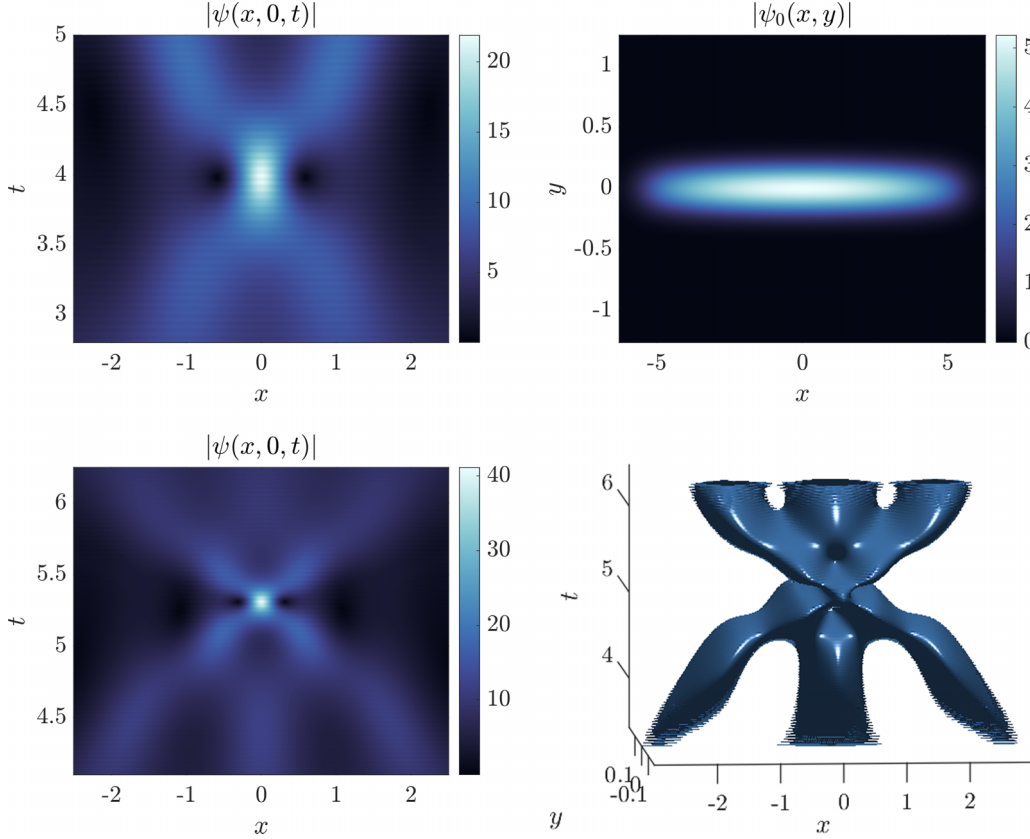
FIG. 3. Top panels: A two-dimensional simulation showing second order rogue wave-type behavior and the highly anistropic nature of the initial condition. The parameters used here are $\Omega_x = 1$, $\Omega_y = 60$, $\mu = 42.7$, $g_{\text{defocus}} = 1$, and $g_{\text{focus}} = -0.05$. Bottom panels: Third-order rogue wave-type behavior. The parameters used here are $\Omega_x = 0.75$, $\Omega_y = 100$, $\mu = 71.1$, $g_{\text{defocus}} = 1$, and $g_{\text{focus}} = -0.05$. An isosurface of constant value 55 displays the profile, in absolute-value squared, of the dynamics.

IV. HIGHER-DIMENSIONAL GENERALIZATIONS

Extending considerations to two spatial dimensions, we are able to observe HORWs, e.g., with $k = 2$ or $k = 3$ in anisotropic variants of the latter setting. More concretely, we show the formation of focusing strongly reminiscent of a second-order rogue wave in the top panel of Fig. 3. In analogy with our one-dimensional protocol, we start from the defocusing NLS regime of the form

$$i\partial_t \psi = -\frac{1}{2}\Delta\psi + g|\psi|^2\psi + V(\mathbf{r})\psi, \qquad (4)$$

with $x \in \mathbb{R}^d$ and $d = 2, 3$. It is clear here that we need an experimentally accessible, highly anisotropic two-dimensional (2D) trap $V(x, y) = \frac{\Omega_x^2}{2}x^2 + \frac{\Omega_y^2}{2}y^2$ to achieve the relevant dynamics. We further show the shape of the initial condition, i.e., the ground state of the defocusing problem with $g = g_{\text{defocus}}$ used to illustrate the level of anisotropy used to ensure the prevention of finite-time blowup of the dynamics. Similarly to our 1D protocol, at $t = 0$, we switch $g = g_{\text{focus}}$. During the subsequent focusing dynamics, we release the trap in the x direction while maintaining the trap in the transverse, that is, y direction fixed. In the bottom panel of Fig. 3, we show the formation of a $k = 3$ rogue wave, as well as an isosurface of the two-dimensional dynamics.

In three spatial dimensions, anisotropy can once again serve to mitigate the risk of collapse, as is well known, e.g., from works such as [51–53]. This, in turn, enables us, within

the regimes of sufficiently tightly transversely confined BECs discussed therein, to identify parameters that lead to a genuine second order rogue wave-type scenario.

This is shown in Fig. 4 both at the level of the quasi-1D space-time evolution (left panel) and at that of the detailed comparison of the main feature in a quasi-1D integrated form with the second-order rogue wave of Eq. (2). In Appendix A, we show that the generated three-dimensional (3D) HORW in Fig. 4 is robust under losses as modeled via three-body interactions [46].

It is worthwhile to point out that such a higher-dimensional (indeed 3D with a tight transverse confinement) protocol has been realized experimentally in the work of [54]. In the latter work, the anisotropic confinement evaded the possibility of collapse and led to the creation of higher-order solitary waves. Our multiparametric exploration suggests that, under suitable parametric selection, it is possible for this protocol to lead to the generation of higher-order rogue waves.

V. CONCLUSIONS AND FUTURE CHALLENGES

In the present work we revisited the framework of higher-order rogue waves that was recently developed in the mathematical literature (via Darboux transformations and robust inverse scattering methods) as a *nongeneric, yet well-accessible* form of wave breaking. While, to the best of our knowledge, this setup has not been explored at the level
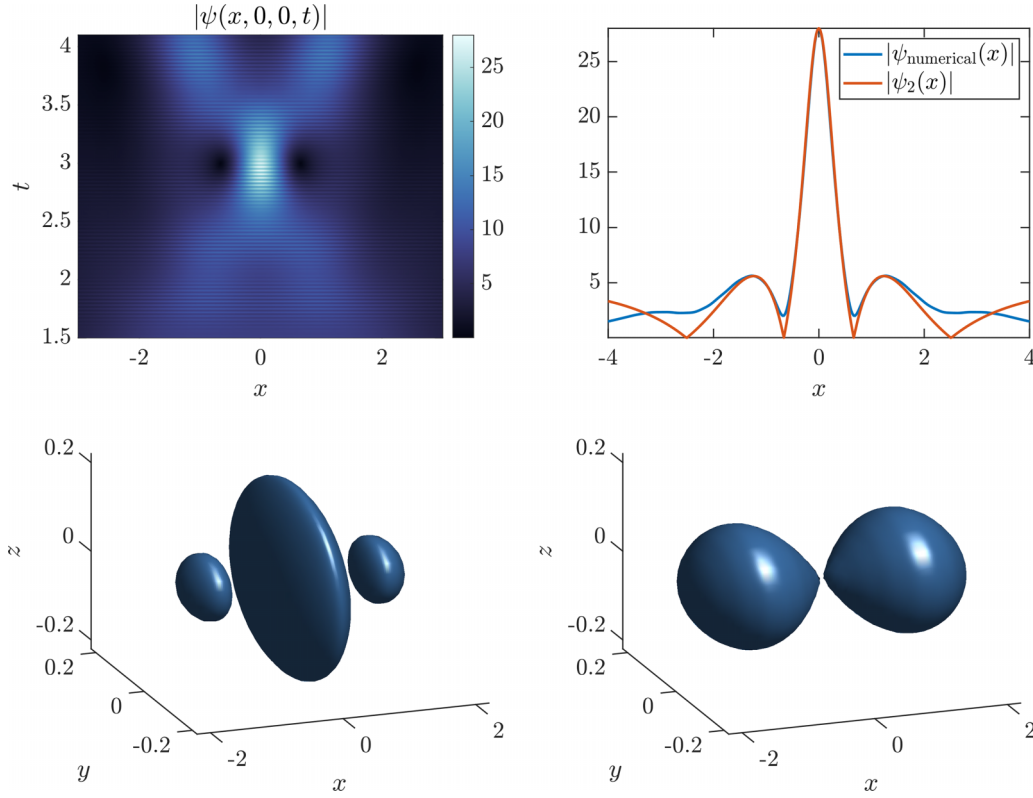
FIG. 4. A three-dimensional simulation that yields a second-order rogue wave-type behavior performed from a defocusing ground state prepared with $\Omega_x = 1$, $\Omega_y = \Omega_z = 100$, $\mu = 143$, and a defocusing coefficient of $g_{\text{defocus}} = 1$. The top left panel shows the space-time evolution for $g_{\text{focus}} = -0.05$ in the elongated direction x. The top right panel shows a corresponding comparison of the central feature with the second-order rogue wave of Eq. (2). The bottom panels are three-dimensional isosurfaces revealing the focusing structure at time 3 in absolute-value 12 (left) and time 4.2 in absolute-value 20 (right).

of realistic or experimentally relevant settings, we showcase examples that are *fully accessible* to current atomic BEC experiments (and also potentially elsewhere, such as, e.g., suitably designed optical media).

We then went on to explore the freedom available to the system through a variation of parameters to provide scenarios enabling the realization of $k = 1$ through $k = 4$ rogue waves, with a view towards higher-order rogue waves, including the intriguing infinite-order one of [38]. While the relevant idea is, in its essence, tailored to one spatial dimension, we illustrate that higher-dimensional, highly anisotropic settings are also accessible and conducive towards such considerations.

Naturally, this study paves the way for numerous further considerations of related concepts. We only mention a few of these here. One necessity is a wide parametric mapping of the space of possible outcomes of near-semi-circular initial data in the space of (μ, Ω) and so on. Another question: how amenable are nonintegrable systems to such types of wave breaking? For example, will HORW-type behavior survive in quintic, cubic-quintic, or other recently proposed so-called droplet [55] variants of the model? A further direction stems from spatially discrete models and concerns whether a variant of such higher-order (including infinite-order [38]) rogue waves exists of Ablowitz-Ladik-type and discrete nonlinear Schrödinger-type lattices [56,57].

It can thus be inferred that this theme presents a wide palette of opportunities in one and higher spatial dimensions

that are extremely timely and relevant for near-future analytical, numerical and experimental considerations.

DATA AVAILABILITY

The data that support the findings of this article are not publicly available. The data are available from the author upon reasonable request.

APPENDIX A: ROBUSTNESS STUDIES

Here we report three robustness studies of the numerically simulated one-dimensional HORWs reported in the main text. The first study we conduct is as follows. We randomly perturb each component of the optimal parameter vector p^*,
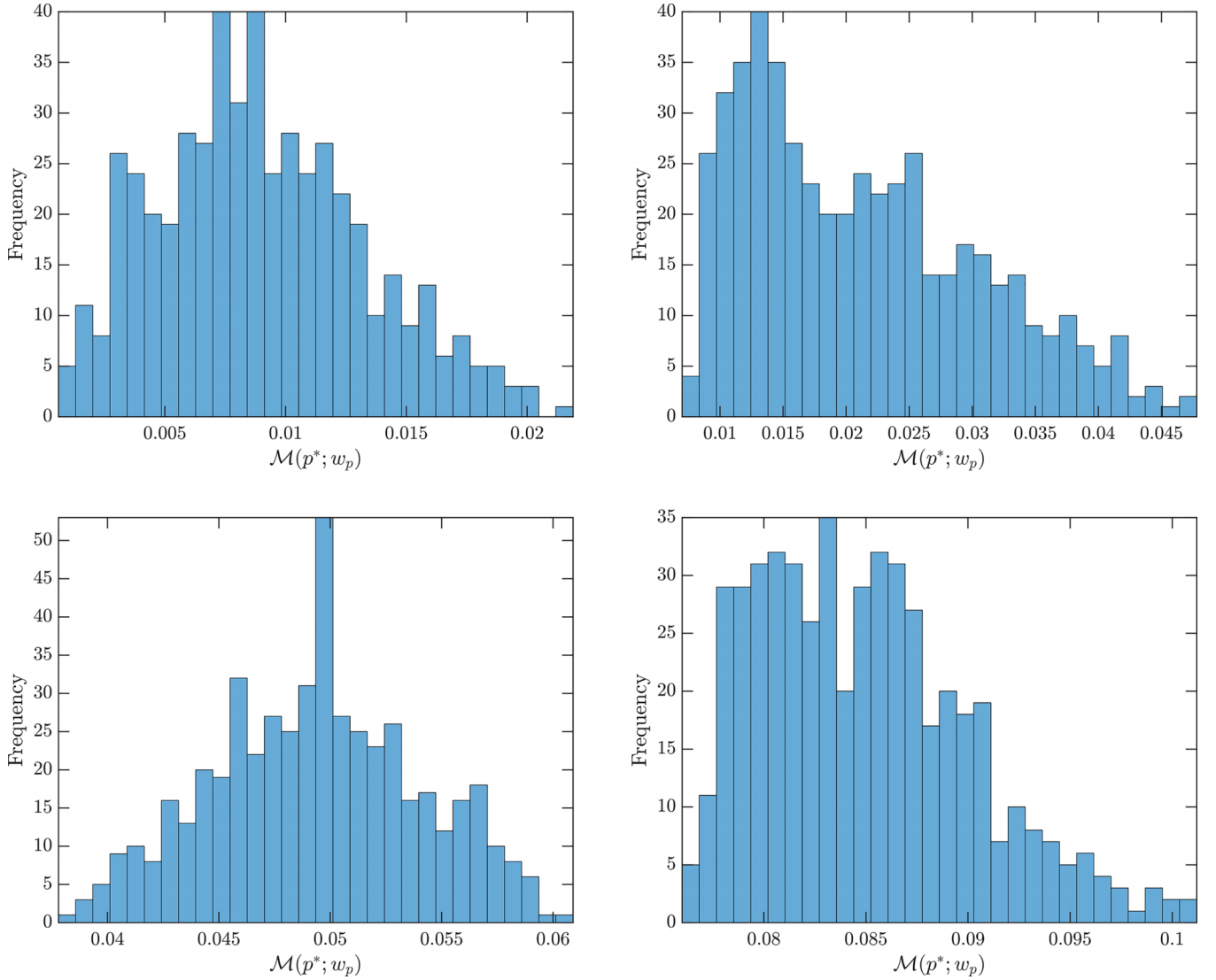
FIG. 5. Histogram plots of the realized mismatches for perturbed parameters $p^* + w_p$ (with a 1% uncertainty) corresponding with Fig. 2 in the main text. Top left: $k = 1$. Top right: $k = 2$. Bottom left: $k = 3$. Bottom right: $k = 4$.

for the parameters reported in the caption of Fig. 2, by at most 1% of each parameter value using uniform sampling. In Fig. 5, we show a histogram plot for the realized mismatches $\mathcal{M}(p^*, w_p)$, where w_p is the realized noise such that each component of the vector $p + w_p$ is within 1% of their respective values. We then repeat the same study for an uncertainty of 10%, omitting the histogram in this case for brevity. We report the histogram at 1% to show that the numerical realizations shown in Fig. 6 are not at the extreme of the left tail of the empirical distribution of HORW realizations.

The main conclusion that we draw here is that, especially for lower-order rogue waves, small perturbations do not significantly shift the mismatch, i.e., nearby parameters yield similarly favorable mismatches. However, even when the mismatches tend to be large, especially at the level of 10% uncertainty, we still observe that the HORWs retain their overall shape. Our numerics predict that these generated HORWs would remain significantly detectable in an experimental setting despite the relatively large uncertainty in the tuning parameters of the scheme. In Fig. 6, we show a few

realizations of the resulting 1% perturbed HORW against their zero noise counterparts from Fig. 2. We also show the resulting 10% perturbed HORW against their zero noise counterparts in Fig. 7.

The second study we conduct considers three-body losses. We model these effects when the focusing dynamics take place, as this is where the losses become most relevant due to the extreme focusing. The focusing dynamics we consider are given by

$$i\partial_t \psi = -\frac{1}{2}\Delta\psi - g_{\text{focus}}|\psi|^2\psi - iK_3|\psi|^4\psi. \quad \text{(A1)}$$

In Fig. 8 we show the functional dependence of the mismatch on the parameter K_3. In Fig. 9, we show examples of how the losses impact the focusing of the dynamics into each HORW in one dimension. We also show the impact of the losses in a three-dimensional scenario in Fig. 10.

It should be kept in mind when considering these figures that, using realistic numbers such as those of [46], the dimensionless value of K_3 turns out to be quite low, roughly about 10^{-3}–10^{-4} for the setup reported in [46]. Hence, we
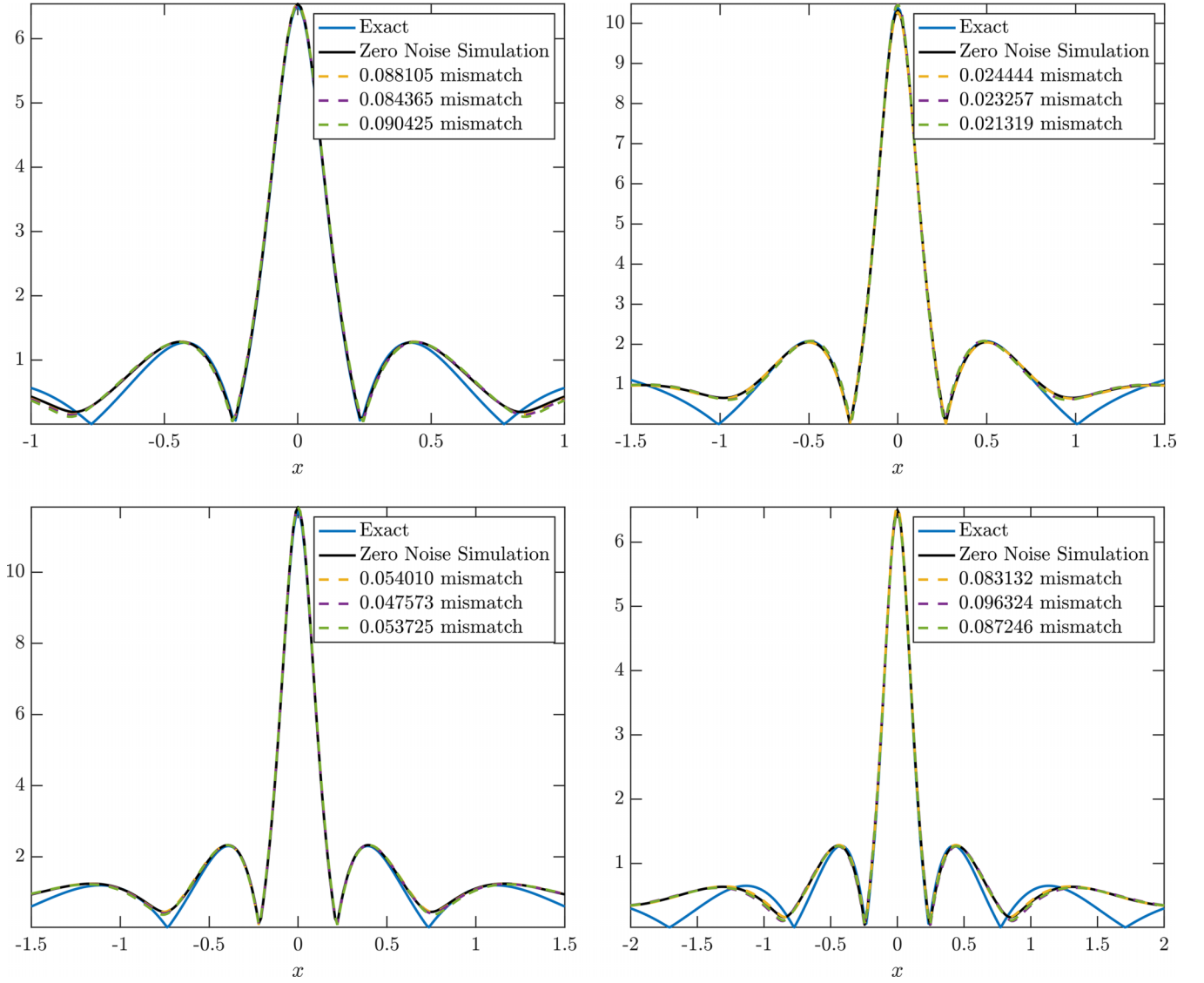
FIG. 6. Three realizations, in absolute-value, of HORWs, sequentially in order, generated from $p^* + w_p$ at 1% of uncertainty, and corresponding with Fig. 2 in the main text. Top left: $k = 1$. Top right: $k = 2$. Bottom left: $k = 3$. Bottom right: $k = 4$.

expect the modification of the reported mismatch and the relevant profile variation to be rather minimal based on the data of Figs. 8 and 9. In general, however, it should be also observed that even for much more substantial values of the dissipation, the relevant graphs of Figs. 9 and 10 are qualitatively quite similar to the ones without the damping effects and hence our phenomenology is fairly robust under the presence of realistic three-body losses.

To further probe robustness of the one-dimensional HORW scenarios against small, structure-preserving fluctuations, we perform a third test involving a random perturbation in the spirit of the zero-temperature truncated-Wigner (TW) approximation [58–61] around the numerically computed stationary state $\phi(x)$ of the defocusing GPE in a harmonic trap. The TW perturbations are constructed in the Bogoliubov–de Gennes (BdG) basis and then the ensuing dynamics are evolved under the *trap-free, focusing* NLS used in the main text.

With $H_0 = -\frac{1}{2}\partial_x^2 + V(x)$ and chemical potential μ the discrete BdG operator is

$$\mathcal{L}_{\mathrm{BdG}} = \begin{pmatrix} H_0 - \mu + 2g_{\mathrm{defocus}}|\phi|^2 & g_{\mathrm{defocus}}\,\phi^2 \\ -g_{\mathrm{defocus}}\,\overline{\phi}^2 & -H_0 + \mu - 2g_{\mathrm{defocus}}|\phi|^2 \end{pmatrix}.$$

We compute M eigenpairs $\{(u_j, v_j, \omega_j)\}_{j=1}^{M}$ with eigenvalues ω_j and enforce the Krein (symplectic) normalization

$$\int (|u_j|^2 - |v_j|^2)\,dx = 1$$
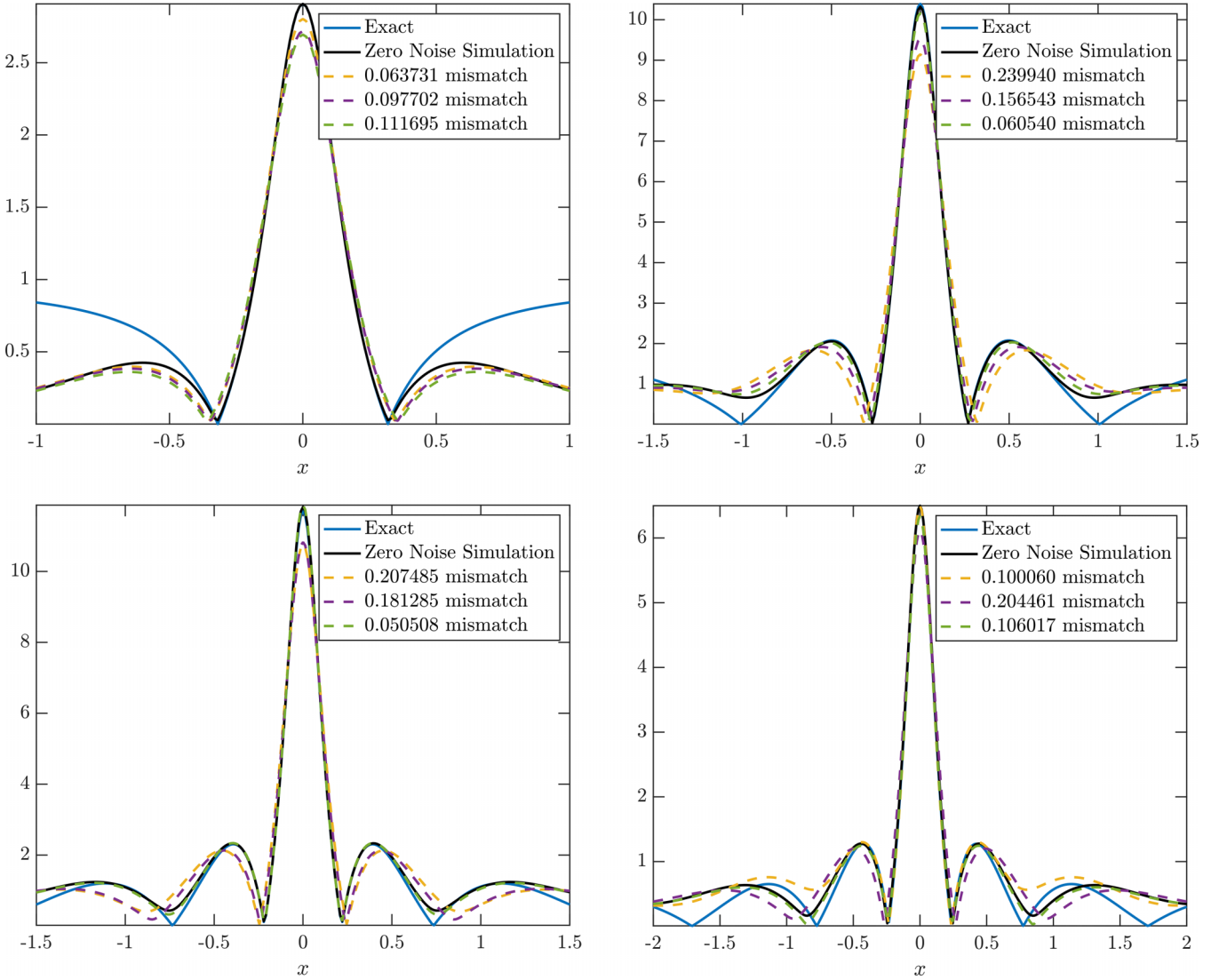
(see [62] for further background).

FIG. 7. Three realizations, in absolute-value, of HORWs, sequentially in order, generated from $p^* + w_p$ at 10% of uncertainty, and corresponding with Fig. 2 in the main text. Top left: $k = 1$. Top right: $k = 2$. Bottom left: $k = 3$. Bottom right: $k = 4$. Despite the larger changes in the mismatch, as compared with Fig. 7, the excited rogue waves maintain their overall shape.

At $T = 0$, half a quantum is added per retained coherent mode. To this end, we sample independent complex Gaussians $\eta_j \sim \mathcal{N}_{\mathbb{C}}(0, \frac{1}{2})$ and form the fluctuation

$$\delta\psi(x) = \sum_{j=1}^{M} (\eta_j u_j(x) + \eta_j^* \overline{v_j(x)}).$$

In our computational realization, we wish to control the level of the overall perturbation while preserving per-mode statistics. With that in mind, we apply a single global scale s chosen so that the *expected* noise mass is a fixed fraction $f \in (0, 1)$ of the condensate mass. That is, we compute the expected value

$$\mathbb{E} \|\delta\psi\|_{L^2}^2 = \frac{1}{2} \sum_{j=1}^{M} \int (|u_j|^2 + |v_j|^2)\, dx,$$

and use $s^2 = f \frac{\|\phi\|_{L^2}^2}{\mathbb{E} \|\delta\psi\|_{L^2}^2}$, to realize each initialization by

$$\psi_0(x) = \phi(x) + s\,\delta\psi(x),$$

We then evolve each realization in trap-free and focusing regime using the split-step Fourier scheme described in Appendix B.

We use an ensemble size of 100 realizations with each realization perturbed by 200 BdG modes. Our results are shown in Fig. 11. There, we show that at sufficiently small BdG-TW perturbation levels, the gross HORW morphology remains intact, even when the expected noise mass is 5% ($f = 0.05$) of the initial condensate mass. In the figure, the perturbation is performed about the optimal ground state leading to the generation the second-order rogue wave.

APPENDIX B: GPE SIMULATION TECHNIQUE

To simulate the lossy GPE (A1), we use a standard operator splitting technique. That is, we rewrite Eq. (A1) as
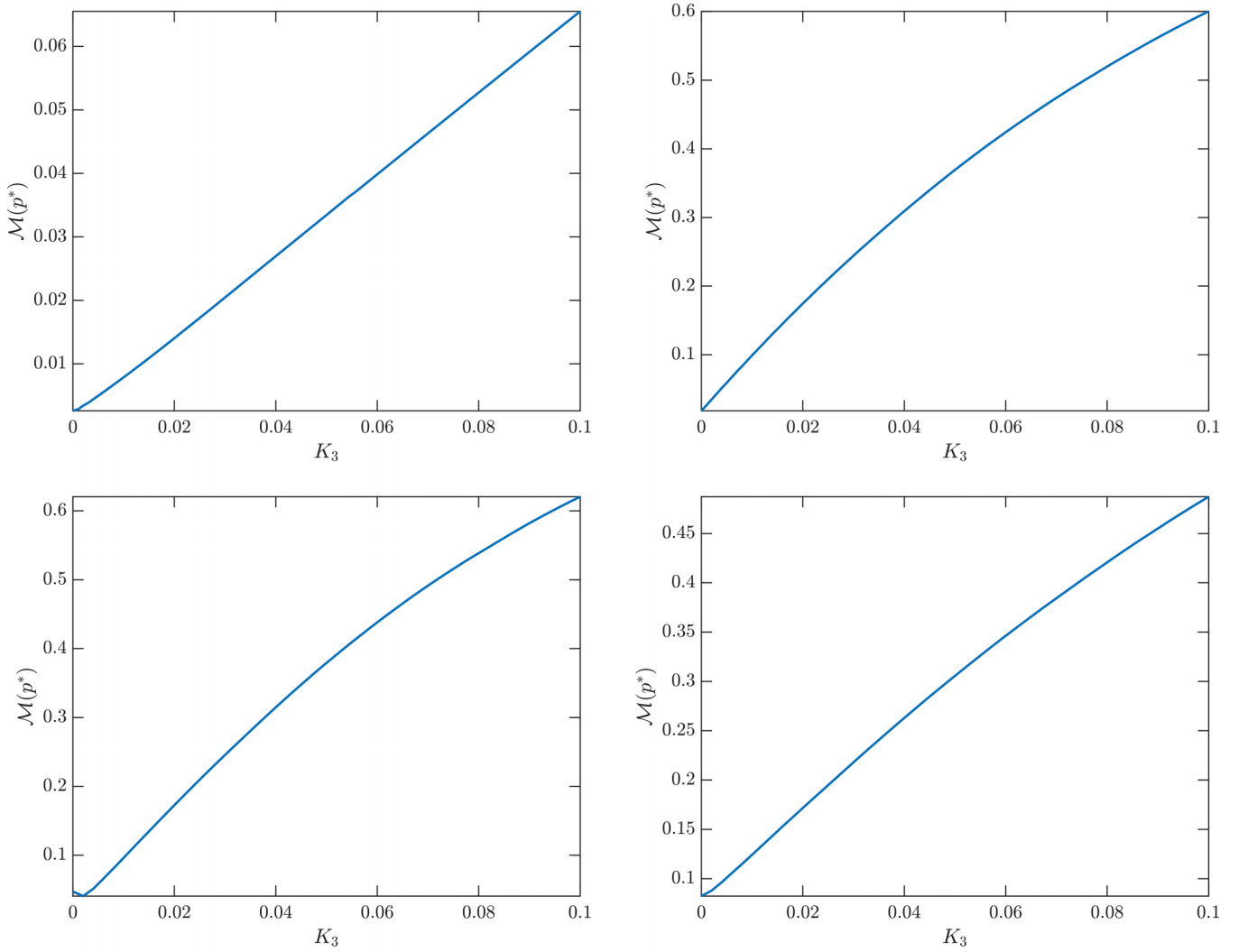
$$i\partial_t = \mathcal{L}\psi + \mathcal{N}(\psi),$$

FIG. 8. Functional dependence of the mismatch on the parameter K_3 from losses as modeled by Eq. (A1). The optimal parameter vector p^* is the one reported in Fig. 2. Top left: $k = 1$. Top right: $k = 2$. Bottom left: $k = 3$. Bottom right: $k = 4$.

where

$$\mathcal{L}\psi = -\tfrac{1}{2}\Delta\psi, \quad \mathcal{N}(\psi) = -g|\psi|^2\psi - iK_3|\psi|^4\psi.$$

We diagonalize the matrix exponential of the linear operator numerically via fast Fourier or inverse Fourier transforms.

The nonlinearity $\mathcal{N}(\psi)$ can be handled using basic quadrature techniques. First, we use polar coordinates, that is,

$$\psi = \rho e^{i\theta}.$$

The resulting equations for the phase and amplitude are

$$\dot{\theta} = g\rho^2, \quad \dot{\rho} = -K_3\rho^5.$$

Integrating the equation for the amplitude from t_n to t_{n+1} is done exactly;

$$\rho_{n+1} = \frac{\rho_n}{\sqrt[4]{1 + 4K_3 h_n \rho_n}},$$

where h_n is the step size $t_{n+1} - t_n$. Integrating the equation for the phase can be handled using the trapezoidal rule

$$\theta_{n+1} = \theta_n + g\int_{t_n}^{t_{n+1}} \rho^2(s)ds = \theta_n + \frac{gh_n}{2}\left(\rho_{n+1}^2 + \rho_n^2\right) + \mathcal{O}\left(h_n^3\right).$$

Simplifying using the fact that $\rho_n = |\psi_n|$ and $\theta_n = \text{Arg } \psi_n$, we have the locally third-order in time update

$$\psi_{n+1} = \rho_{n+1}e^{i\theta_{n+1}},$$

where

$$\rho_{n+1} = \frac{|\psi_n|}{\sqrt[4]{1 + 4K_3 h_n|\psi_n|}},$$

$$\theta_{n+1} = \text{Arg}\psi_n + \frac{gh_n}{2}|\psi_n|^2(1 + (1 + 4K_3 h_n|\psi_n|)^{-1/2}).$$

Note that when $K_3 = 0$, the nonlinear update reduces to

$$\rho_{n+1} = |\psi_n|, \quad \theta_{n+1} = \text{Arg } \psi_n + gh_n|\psi_n|^2,$$

and is exact within the evaluation of the matrix operator of the nonlinearity. This scheme is what is used in the numerical solution of the focusing and trap-free ($V \equiv 0$) version of Eq. (4).

To make the method adaptive and globally third order in time for the efficient resolution of the transient and extreme focusing that we observe throughout this work, we use a combination of Strang splitting and Richardson extrapolation;
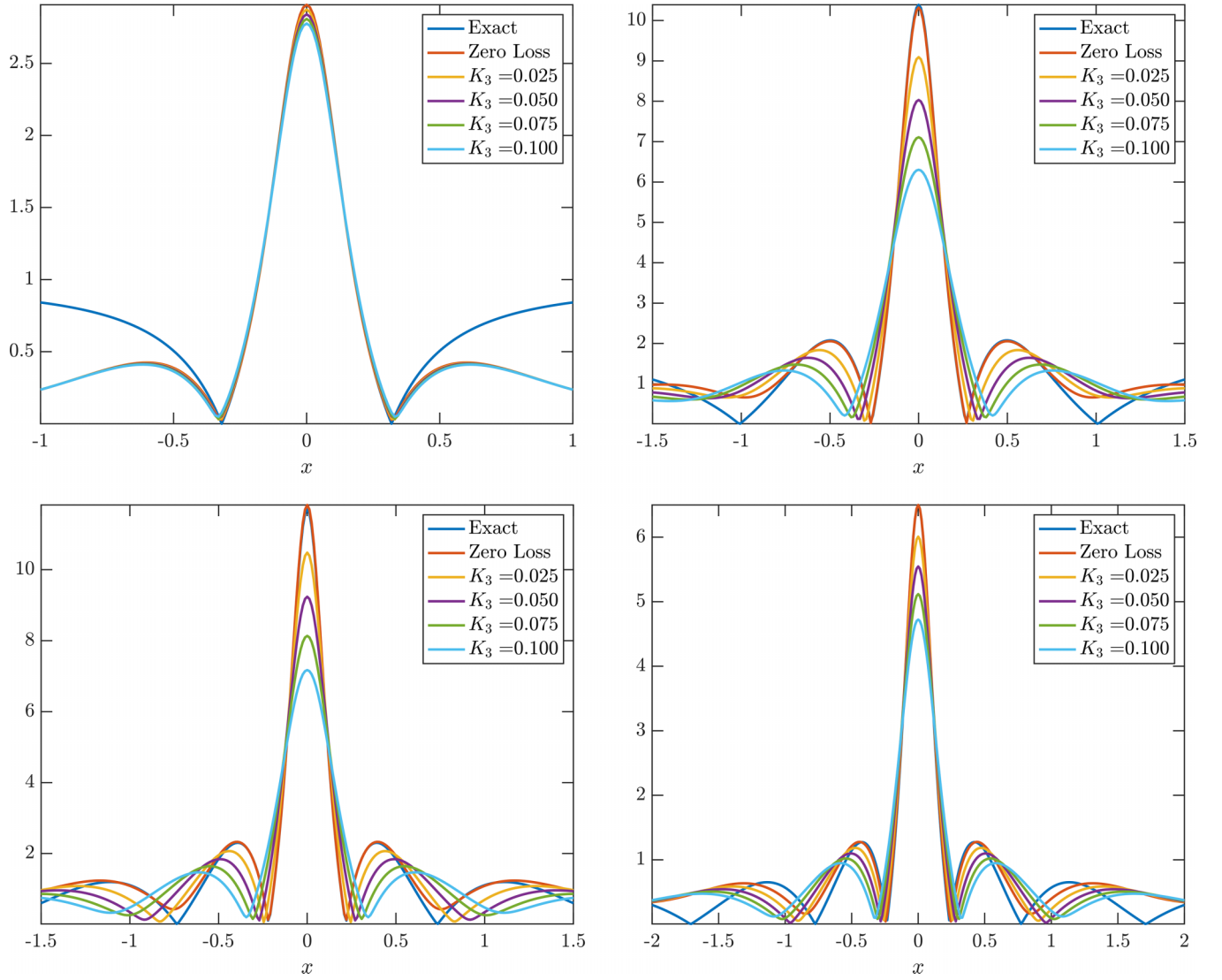
FIG. 9. Realized HORWs for different values of K_3 from losses as modeled by Eq. (A1). The zero loss cases are the ones reported in Fig. 2. Top left: $k = 1$. Top right: $k = 2$. Bottom left: $k = 3$. Bottom right: $k = 4$.
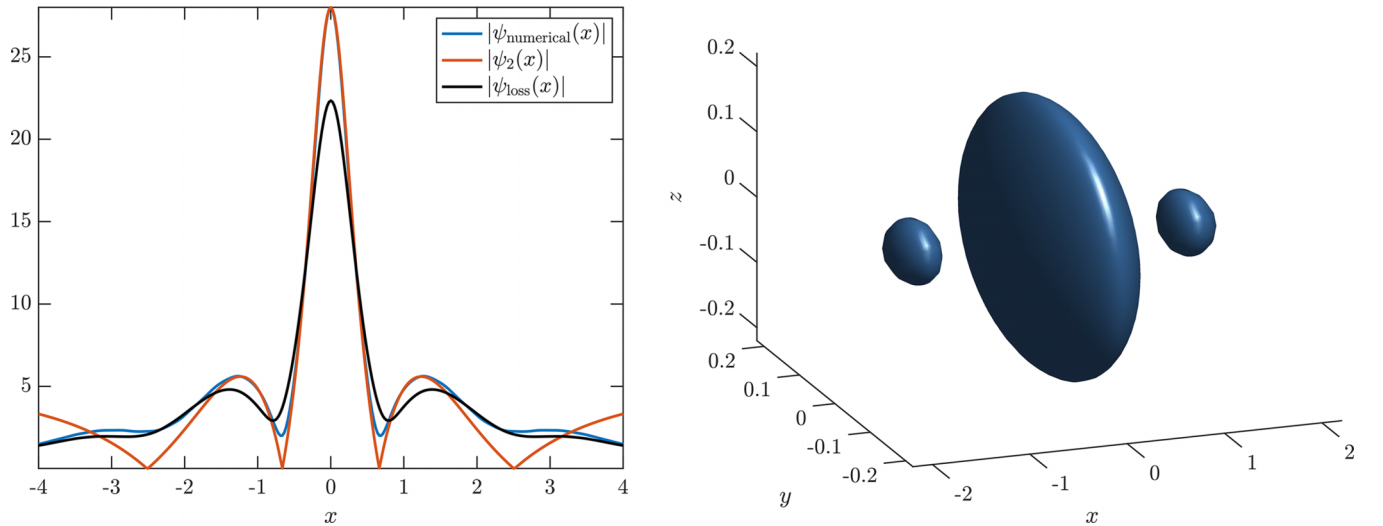

FIG. 10. Realized second-order rogue wave with a loss modeled by Eq. (A1). The parameter $K_3 = 0.005$ shows that a relatively small loss does not distort the shape of the generated rogue wave drastically. The isocontour on the right was set to 12, consistent with the zero loss case shown in Fig. 4.
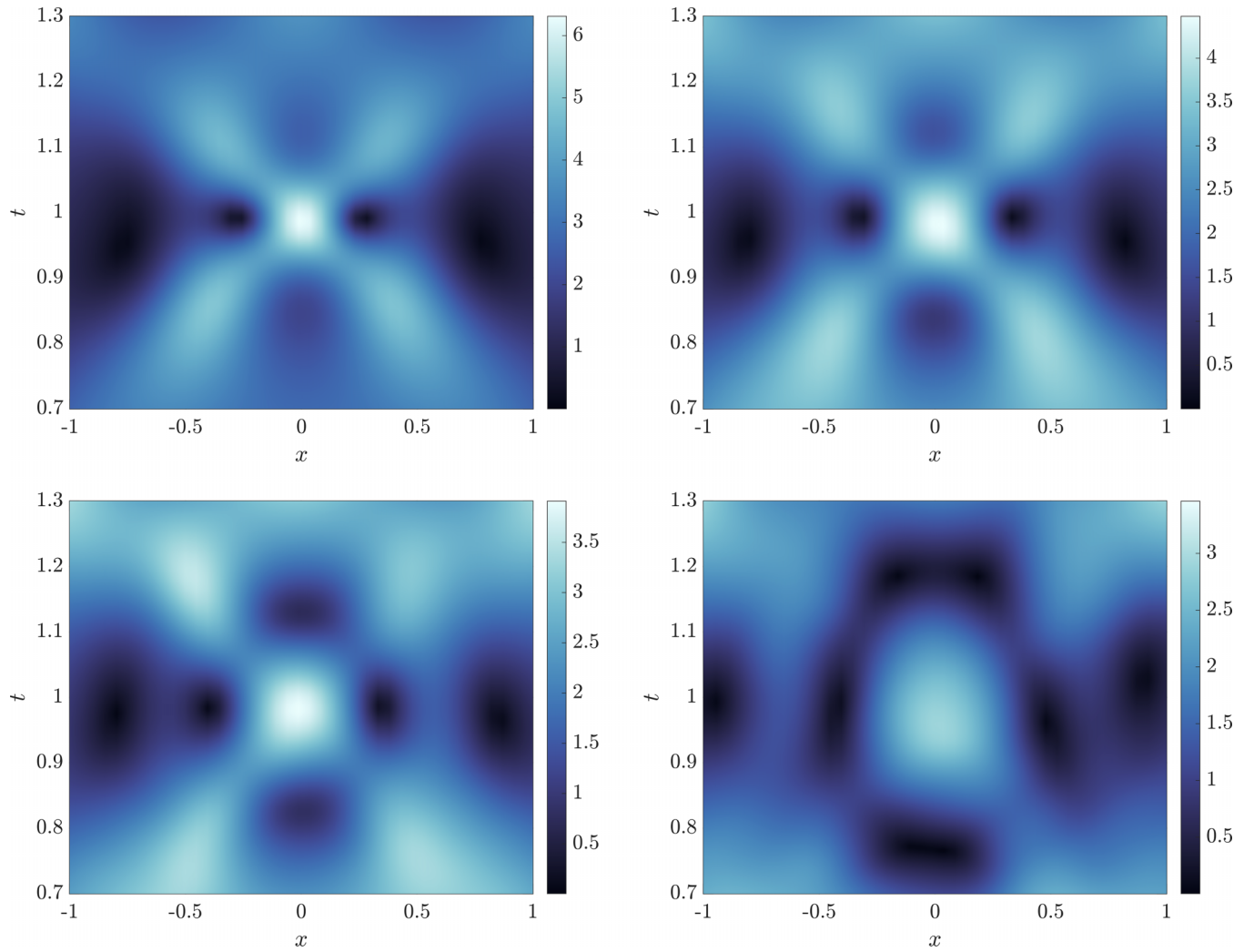
FIG. 11. An ensemble average over 100 realizations in the spirit of the TW approximation (see the detailed explanation in the text). Top left: $f = 0.001$. Top right: $f = 0.005$. Bottom left: $f = 0.01$. Bottom right: $f = 0.05$.

see [49] for an excellent explanation of this method. We use a similar strategy to compute the ground state of the defocusing equation using a renormalized imaginary time propagation method; please see [48] for more details.

[1] Z. Yan, J. Phys.: Conf. Ser. **400**, 012084 (2012).

[2] M. Onorato, S. Residori, U. Bortolozzo, A. Montina, and F. T. Arecchi, Phys. Rep. **528**, 47 (2013).

[3] J. M. Dudley, F. Dias, M. Erkintalo, and G. Genty, Nat. Photon. **8**, 755 (2014).

[4] D. Mihalache, Rom. Rep. Phys **69**, 403 (2017).

[5] J. M. Dudley, G. Genty, A. Mussot, A. Chabchoub, and F. Dias, Nat. Rev. Phys. **1**, 675 (2019).

[6] A. Tikan, S. Randoux, G. El, A. Tovbis, F. Copie, and P. Suret, Front. Phys. **8**, 599435 (2021).

[7] D. R. Solli, C. Ropers, P. Koonath, and B. Jalali, Nature (London) **450**, 1054 (2007).

[8] D. R. Solli, C. Ropers, and B. Jalali, Phys. Rev. Lett. **101**, 233902 (2008).

[9] B. Kibler, J. Fatome, C. Finot, G. Millot, F. Dias, G. Genty, N. Akhmediev, and J. M. Dudley, Nat. Phys. **6**, 790 (2010).

[10] B. Kibler, J. Fatome, C. Finot, G. Millot, G. Genty, B. Wetzel, N. Akhmediev, F. Dias, and J. M. Dudley, Sci. Rep. **2**, 463 (2012).

[11] P. T. S. DeVore, D. R. Solli, D. Borlaug, C. Ropers, and B. Jalali, J. Opt. **15**, 064001 (2013).

[12] B. Frisquet, B. Kibler, P. Morin, F. Baronio, M. Conforti, G. Millot, and S. Wabnitz, Sci. Rep. **6**, 20785 (2016).

[13] A. Tikan, C. Billet, G. El, A. Tovbis, M. Bertola, T. Sylvestre, F. Gustave, S. Randoux, G. Genty, P. Suret, and J. M. Dudley, Phys. Rev. Lett. **119**, 033901 (2017).

[14] A. Chabchoub, N. P. Hoffmann, and N. Akhmediev, Phys. Rev. Lett. **106**, 204502 (2011).

[15] A. Chabchoub, N. Hoffmann, M. Onorato, and N. Akhmediev, Phys. Rev. X **2**, 011015 (2012).

[16] A. Chabchoub and M. Fink, Phys. Rev. Lett. **112**, 124101 (2014).

[17] D. H. Peregrine, J. Aust. Math. Soc. Series B Appl. Math. **25**, 16 (1983).

[18] H. Bailung, S. K. Sharma, and Y. Nakamura, Phys. Rev. Lett. **107**, 255005 (2011).

[19] R. Sabry, W. M. Moslem, and P. K. Shukla, Phys. Plasmas **19**, 122903 (2012).

[20] R. E. Tolba, W. M. Moslem, N. A. El-Bedwehy, and S. K. El-Labany, Phys. Plasmas **22**, 043707 (2015).

[21] A. Romero-Ros, G. C. Katsimiga, S. I. Mistakidis, S. Mossman, G. Biondini, P. Schmelcher, P. Engels, and P. G. Kevrekidis, Phys. Rev. Lett. **132**, 033402 (2024).

[22] T. Claeys and T. Grava, Commun. Math. Phys. **286**, 979 (2009).

[23] M. Bertola and A. Tovbis, Commun. Pure Appl. Math. **66**, 678 (2013).

[24] B.-Y. Lu and P. Miller, Commun. Pure Appl. Math. **75**, 1517 (2022).

[25] Y. S. Kivshar and G. P. Agrawal, *Optical Solitons: From Fibers to Photonic Crystals* (Academic, New York, 2003), pp. 1–540.

[26] A. Hasegawa and Y. Kodama, *Solitons in Optical Communications* (Clarendon, Oxford, 1995).

[27] L. Pitaevskii and S. Stringari, *Bose-Einstein Condensation* (Oxford University Press, Oxford, UK, 2003).

[28] C. J. Pethick and H. Smith, *Bose–Einstein Condensation in Dilute Gases* (Cambridge University Press, Cambridge, England, 2002).

[29] P. G. Kevrekidis, D. J. Frantzeskakis, and R. Carretero-González, *The Defocusing Nonlinear Schrödinger Equation* (SIAM, Philadelphia, 2015).

[30] M. Kono and M. Skorić, *Nonlinear Physics of Plasmas* (Springer, Heidelberg, Germany, 2010).

[31] V. I. Talanov, JETP Lett. **11**, 199 (1970).

[32] A. V. Gurevich and A. B. Shvartsburg, J. Exp. Theor. Phys. **31**, 1084 (1970).

[33] F. Demontis, G. Ortenzi, G. Roberti, and M. Sommacal, Phys. Rev. E **108**, 024213 (2023).

[34] J. S. He, H. R. Zhang, L. H. Wang, K. Porsezian, and A. S. Fokas, Phys. Rev. E **87**, 052914 (2013).

[35] D. Bilman, L. Ling, and P. D. Miller, Duke Math. J. **169**, 671 (2020).

[36] D. Bilman and P. D. Miller, Physica D **435**, 133289 (2022).

[37] N. Akhmediev, Front. Phys. **8**, 612318 (2021).

[38] B. Suleimanov, JETP Lett. **106**, 400 (2017).

[39] G. Karali and C. Sourdis, Arch. Ration. Mech. Anal. **217**, 439 (2015).

[40] C. Gallo and D. E. Pelinovsky, Asymptot. Anal. **73**, 53 (2009).

[41] S. L. Cornish, N. R. Claussen, J. L. Roberts, E. A. Cornell, and C. E. Wieman, Phys. Rev. Lett. **85**, 1795 (2000).

[42] J. L. Roberts, N. R. Claussen, S. L. Cornish, E. A. Donley, E. A. Cornell, and C. E. Wieman, Phys. Rev. Lett. **86**, 4211 (2001).

[43] S. E. Pollack, D. Dries, M. Junker, Y. P. Chen, T. A. Corcovilos, and R. G. Hulet, Phys. Rev. Lett. **102**, 090402 (2009).

[44] C.-A. Chen and C.-L. Hung, Phys. Rev. Lett. **125**, 250401 (2020).

[45] Y. V. Bludov, V. V. Konotop, and N. Akhmediev, Phys. Rev. A **80**, 033610 (2009).

[46] S. Banerjee, K. Zhou, S. K. Tiwari, H. Tamura, R. Li, P. G. Kevrekidis, S. I. Mistakidis, V. Walther, and C.-L. Hung, Phys. Rev. Lett. **135**, 073401 (2025).

[47] E. A. Donley, N. R. Claussen, S. L. Cornish, J. L. Roberts, E. A. Cornell, and C. E. Wieman, Nature (London) **412**, 295 (2001).

[48] W. Bao and Q. Du, J. Sci. Comput. **25**, 1674 (2004).

[49] O. V. Sinkin, R. Holzlöhner, J. Zweck, and C. R. Menyuk, J. Lightwave Technol. **21**, 61 (2003).

[50] R. Storn and K. Price, J. Global Optim. **11**, 341 (1997).

[51] V. M. Pérez-García, H. Michinel, J. I. Cirac, M. Lewenstein, and P. Zoller, Phys. Rev. A **56**, 1424 (1997).

[52] L. Salasnich, A. Parola, and L. Reatto, Phys. Rev. A **66**, 043603 (2002).

[53] E. E. C. Márquez, Bright solitons in a quasi-one-dimensional dipolar Bose-Einstein condensate, Master's thesis, Universidade Estadual Paulista Júlio de Mesquita Filho, Instituto de Física Teórica, São Paulo, 2014.

[54] A. Di Carli, C. D. Colquhoun, G. Henderson, S. Flannigan, G.-L. Oppo, A. J. Daley, S. Kuhr, and E. Haller, Phys. Rev. Lett. **123**, 123602 (2019).

[55] Z.-H. Luo, W. Pang, B. Liu, Y.-Y. Li, and B. A. Malomed, Front. Phys. **16**, 32201 (2021).

[56] M. Ablowitz, B. Prinari, and A. Trubatch, *Discrete and Continuous Nonlinear Schrödinger Systems* (Cambridge University Press, Cambridge, England, 2004).

[57] P. G. Kevrekidis, *The Discrete Nonlinear Schrödinger Equation* (Springer, Berlin, 2009).

[58] M. J. Steel, M. K. Olsen, L. I. Plimak, P. D. Drummond, S. M. Tan, M. J. Collett, D. F. Walls, and R. Graham, Phys. Rev. A **58**, 4824 (1998).

[59] A. Sinatra, C. Lobo, and Y. Castin, J. Phys. B: At. Mol. Opt. Phys. **35**, 3599 (2002).

[60] P. B. Blakie, A. S. Bradley, M. J. Davis, R. J. Ballagh, and C. W. Gardiner, Adv. Phys. **57**, 363 (2008).

[61] N. P. Proukakis and B. Jackson, J. Phys. B: At. Mol. Opt. Phys. **41**, 203002 (2008).

[62] A. L. Fetter, Rev. Mod. Phys. **81**, 647 (2009).